Inorganic Chemistry

Article

pubs.acs.org/IC

Lead-Free $MA_2CuCl_xBr_{4-x}$ Hybrid Perovskites

Daniele Cortecchia,[†,‡] Herlina Arianita Dewi,[‡] Jun Yin,[§] Annalisa Bruno,[‡,§] Shi Chen,[§] Tom Baikie,[‡] Pablo P. Boix,[‡] Michael Grätzel,[∥] Subodh Mhaisalkar,[‡,⊥] Cesare Soci,[§] and Nripan Mathews*[,‡,⊥]

[†]Interdisciplinary Graduate School, Energy Research Institute at NTU, 639798 Singapore

[‡]Energy Research Institute @ NTU (ERI@N), Research Technoplaza, Nanyang Technological University, Nanyang Drive, 637553 Singapore

[§]Division of Physics and Applied Physics, Nanyang Technological University, 637371 Singapore

[∥]Laboratory of Photonics and Interfaces, Department of Chemistry and Chemical Engineering, Swiss Federal Institute of Technology, Station 6, Lausanne CH-1015, Switzerland

[⊥]School of Materials Science and Engineering, Nanyang Technological University, Nanyang Avenue, 639798 Singapore

Supporting Information

ABSTRACT: Despite their extremely good performance in solar cells with efficiencies approaching 20% and the emerging application for light-emitting devices, organic−inorganic lead halide perovskites suffer from high content of toxic, polluting, and bioaccumulative Pb, which may eventually hamper their commercialization. Here, we present the synthesis of two-dimensional (2D) Cu-based hybrid perovskites and study their optoelectronic properties to investigate their potential application in solar cells and light-emitting devices, providing a new environmental-friendly alternative to Pb. The series $(CH_3NH_3)_2CuCl_xBr_{4-x}$ was studied in detail, with the role of Cl found to be essential for stabilization. By exploiting the additional Cu d−d transitions and appropriately tuning the Br/Cl ratio, which affects ligand-to-metal charge transfer transitions, the optical absorption in this series of compounds can be extended to the near-infrared for optimal spectral overlap with the solar irradiance. In situ formation of Cu^+ ions was found to be responsible for the green photoluminescence of this material set. Processing conditions for integrating Cu-based perovskites into photovoltaic device architectures, as well as the factors currently limiting photovoltaic performance, are discussed: among them, we identified the combination of low absorption coefficient and heavy mass of the holes as main limitations for the solar cell efficiency. To the best of our knowledge, this is the first demonstration of the potential of 2D copper perovskite as light harvesters and lays the foundation for further development of perovskite based on transition metals as alternative lead-free materials. Appropriate molecular design will be necessary to improve the material's properties and solar cell performance filling the gap with the state-of-the-art Pb-based perovskite devices.

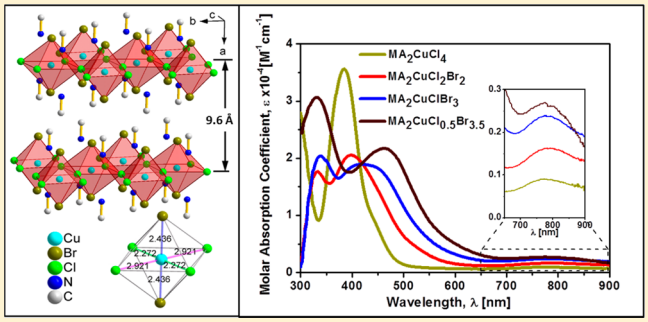

INTRODUCTION

In the past two years, organic−inorganic lead halide perovskites have delivered breakthrough solar cell efficiencies.[1,2] In particular, after the first pioneering works,[3−5] record performances have been demonstrated in succession with methylammonium lead iodide $CH_3NH_3PbI_3$[6−12] thanks to its long electron−hole diffusion length, high absorption coefficient, and low defect density.[13−15] Power conversion efficiencies of 19.3%[16] and NREL-certified 20.1% have been achieved, establishing perovskites as the most efficient solution-processed solar cells, and challenging the thin film and polycrystalline silicon solar cell paradigm.[17−19] Recently, the application of hybrid perovskites have been extended with superlative results to light-emitting devices[20] opening new frontiers for perovskite-based lasers,[14] light-emitting diodes (LEDs),[21] and field-effect light-emitting transistors (FETs).[22] Despite these unprecedented advances[23] and the versatility in fabrication processes,[24] the lead content of these materials[25,26] has raised concerns due to its toxicity[27] and bioaccumulation in the ecosystem,[28] thus hampering the perovskites' pathway to commercialization.

It is therefore of primary importance to study and develop alternative classes of lead-free perovskites for optoelectronic applications.[13] In the photovoltaic community, first attempt to replace Pb^{2+} involved substitution with Sn^{2+},[29−31] and efficiencies as high as 6% were shown with $CH_3NH_3SnI_3$.[32] However, Sn^{2+} is easily oxidized into Sn^{4+}, which is a stumbling block that frustrates reproducibility of highly efficient devices and limits practical use of these compounds. Typically, hybrid perovskite sensitizers are based on the three-dimensional (3D) structure with general formula AMX_3, where X = Cl^-, Br^-, I^-; A is an organic cation like methylammonium $CH_3NH_3^+$ (MA)

Received: August 25, 2015
Published: January 12, 2016

DOI: 10.1021/acs.inorgchem.5b01896
Inorg. Chem. 2016, 55, 1044−1052

and formamidinium $HC(NH_2)_2^+$ (FA); and M is a divalent metal like Sn^{2+} and Pb^{2+}. Here the 3D network is made of a series of corner-sharing MX_6 octahedra with the organic cations occupying the cubohoctahedral cavities, maintaining electroneutrality of the system. However, the necessity of developing sustainable technologies based on environmentally friendly, earth-abundant, and cost-effective materials naturally drives the attention toward the transition metals, where particularly attractive metals (e.g., Fe^{2+}, Cu^{2+}, Zn^{2+}) can be found to investigate potential alternatives to lead-based perovskites. Thanks to their rich chemistry, their use may enormously extend synthetic routes of new perovskites for photovoltaic and light-emitting applications improving the tunability of the material. Because of the smaller ionic radii of transition metals, the 3D structure is sterically hindered, and the atoms rearrange in a layered configuration, which is isostructural to compounds of the Ruddlesden−Popper phase like K_2NiF_4[33] and the high-temperature superconductor $La_{2-x}Ba_xCuO_4$.[34] This two-dimensional (2D) structure can be derived by cutting the standard 3D perovskite along specific orientations (⟨100⟩, ⟨110⟩, and ⟨111⟩) and piling up alternating organic and inorganic slabs.[35] The resulting general formula can be written as $(R\text{-}NH_3)_2A_{n-1}M_nX_{3n+1}$, where n is the number of layers within an inorganic slab.[36,37] Cu^{2+} [electronic configuration $3d^9$ (t_{2g}^6 e_g^3)] is particularly interesting due to the stability of this oxidation state in aerobic environment and the ability to form compounds with large absorption coefficient in the visible region.[38] Moreover, the Jahn−Teller distortion introduces elastic semicoordinate bonds in the inorganic planes, which confers higher flexibility to the structure, resulting in an easier interaction even with larger organoammonium cations and offering wider synthetic tunability.[39] 2D Cu-based perovskites have been previously studied mainly for their interesting magnetic properties,[39,40] whereby they behave like quasi-2D Heisenberg ferromagnets.[41,42] Recently (EDBE)[$CuCl_4$], where EDBE = 2,2′-(ethylenedioxy)bis(ethylammonium), has been applied as cathode material in Li^+ ions batteries.[43] Pb-based systems with lower dimensionality have also recently been studied as sensitizers to improve the stability of these materials against moisture,[44] and the 1D system with perovskite-related structure $(CH_3CH_2NH_3)PbI_3$ was shown to work as sensitizer in solar cells.[45] However, very little is known about the optoelectronic properties of Cu-based hybrid halide perovskites, and no demonstration of photovoltaic action has been reported in this material set. This guided our motivation to study functional Cu-based perovskites for Pb replacement in low-dimensionality systems.

Here, we report the synthesis and characterization of a 2D copper-based hybrid perovskite family with the general formula $(CH_3NH_3)_2CuCl_xBr_{4-x}$ with the aim of investigating the film formation for technological applications and studying the optoelectronic properties to explore their potential as light harvesters in solar cells and their luminescence properties. The presence of Cl^- is essential to improve the material stability against copper reduction and enhance the perovskite crystallization. By changing the Br/Cl ratio, the optical absorption can be tuned within the visible to near-infrared (λ = 300−900 nm) range. Optical transitions and transport properties of this new class of materials were understood and assigned using ab initio calculations based on the density functional theory (DFT). In situ formation of Cu^+ trap states was found to be responsible for an efficient green emission of these perovskites. Thin film fabrication and deposition parameters were also studied to optimize integration of these materials into a photovoltaic device structure. The solar cell performance and the factors currently limiting the efficiency of this device are discussed to provide guidelines for future optimization and investigation of lead-free perovskites.

RESULTS AND DISCUSSION

The fundamental properties of $MA_2CuCl_xBr_{4-x}$ were first studied by synthesizing powders with different Br/Cl ratio. The fully bromine-substituted compound MA_2CuBr_4 was obtained from ethanol only after complete evaporation of the solvent. The Pawley fit of the powder X-ray diffraction pattern was done using the structural parameters previously reported by Y. Kimishima (orthorhombic crystal system and space group *Pbca*)[46] and revealed the presence of some extra peaks between 10 and 28 2θ degrees not belonging to the perovskite, indicating that it was not possible to achieve a high-purity material with this process (Figure S1, Supporting Information). Moreover, the material was extremely deliquescent and sensitive to atmospheric moisture, making it not suitable for further fabrication process. To overcome this issue, we found that the stability of the material can be greatly enhanced for compounds with mixed halides $MA_2CuCl_xBr_{4-x}$, and a little amount of chlorine is enough to greatly improve the crystallization as well as the moisture resistance without compromising the optical properties. Using this strategy, the perovskites crystallized spontaneously from alcoholic solution, and it was possible to synthesize in air high-quality perovskite powders with high Br/Cl molar ratio (up to 7 in the case of $MA_2CuCl_{0.5}Br_{3.5}$). Figure 1a displays the diffractograms of all the chlorine-stabilized powders synthesized $MA_2CuCl_xBr_{4-x}$, and Table 1 summarizes their crystallographic properties. Pawley fits of the powder X-ray diffraction patterns (Figure S2, Supporting Information) were performed using the structural parameters previously reported from single-crystal X-ray diffraction (XRD) of MA_2CuCl_4[47] and $MA_2CuCl_2Br_2$.[48] The extracted lattice parameters show very long-range symmetry along the *c*-axis, which is consistent with the formation of the expected layered structure, and are in good agreement with the values reported previously for the first two compounds of the series.[47,48]

While MA_2CuCl_4 is monoclinic, the materials with mixed halides $MA_2CuCl_2Br_2$, $MA_2CuClBr_3$, and $MA_2CuCl_{0.5}Br_{3.5}$ crystallize with an orthorhombic crystal system. The gradual replacement of Cl with Br can be followed by the shift of all the Bragg reflections, except for the 002, toward smaller angles (Figure S3, Supporting Information). This denotes the increase of unit cell dimension due to the larger effective ionic radius of Br^- (196 pm) compared to Cl^- (181 pm). XRD analysis confirmed the formation of a layered structure having a spacing of ∼10 Å between consecutive inorganic layers, as illustrated for $MA_2CuCl_2Br_2$ in Figure 1b. Cu^{2+} has a highly distorted octahedral coordination CuX_6 (X = Cl, Br), arising from strong Jahn−Teller distortion: two of the four Cu−X bonds located in equatorial position (contained within the inorganic plane) are highly elongated compared to the other four short Cu−X distances. As shown in the inset of Figure 1b, the bond length is 2.272(1) Å for two of the equatorial bonds (green), 2.921(3) Å for the elongated equatorial bonds (pink), and 2.436(2) Å for the terminal bonds (blue). Moreover, in agreement with previous NMR studies,[49] Cl^- preferentially occupies the equatorial positions, while Br^- occupies the apical position of the Cu^{2+} octahedral coordination sphere. Organic and inorganic

DOI: 10.1021/acs.inorgchem.5b01896
Inorg. Chem. 2016, 55, 1044−1052

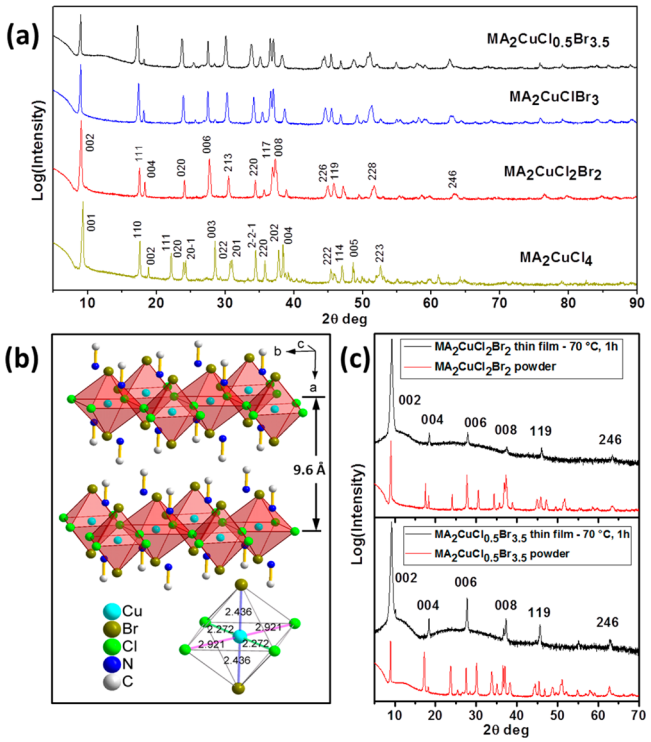

Figure 1. XRD characterization of 2D copper-based perovskites: (a) powder XRD of MA_2CuCl_4 (yellow), $MA_2CuCl_2Br_2$ (red), $MA_2CuClBr_3$ (blue), and $MA_2CuCl_{0.5}Br_{3.5}$ (black); (b) crystal structure of $MA_2CuCl_2Br_2$, showing the alternation of organic and inorganic layers and the Cu−X bond lengths in the inorganic framework (structural data taken from ICSD No. 110677);[48] (c) thin film XRD of $MA_2CuCl_2Br_2$ (upper) and $MA_2CuCl_{0.5}Br_{3.5}$ (lower) compared to their respective powders, showing strong preferential orientation toward the 00l direction.

layers are arranged alternately with the $CH_3NH_3^+$ cations interacting through hydrogen bonds with the halogen atoms of the inorganic layer, while the metal atoms are shifted with respect to adjacent layers in a staggered configuration. The formation of the observed 2D perovskite structure is in agreement with the prediction based on Goldschmidt tolerance factor $\mathbf{t} = \frac{R_A + R_X}{\sqrt{2}(R_M + R_X)}$ and octahedral factor $\mu = \frac{R_M}{R_X}$, where R_A, R_M, and R_X are, respectively, the effective ionic radii of the cations A^+ and M^{2+} and the anion X^-.[50] Empirically it is found that the optimal stability range of the 3D perovskite structure is in the window $0.8 < t < 0.9$ and $0.442 < \mu < 0.895$,[2] where the great majority of 3D perovskite with formula AMX_3 can be found.[51] Assuming the ionic radius of methylammonium R_{MA} = 180 pm,[52] the hypothetical perovskite $MACuCl_3$ will have t = 1.004 and μ = 0.403, clearly out of the stability range and allowing to predict the rearrangement into a perovskite with lower dimensionality, in this case the 2D perovskite MA_2CuCl_4.

These layered perovskites can be easily deposited as films on flat surfaces from a dimethyl sulfoxide (DMSO) solution. $MA_2CuCl_2Br_2$ and $MA_2CuCl_{0.5}Br_{3.5}$ were selected for further optimization by virtue of their better stability and improved optical properties, respectively. Thin-film XRD patterns of these two films are shown in Figure 1c and compared to their respective powders. In both the cases, the 00l reflections are enhanced, and the films show a strong preferential orientation toward the 002 direction, with the organic and inorganic layers parallel to the substrate. The annealing conditions were optimized to obtain crystalline, single-phase films. Thermogravimetric analysis (TGA) showed the beginning of weight loss at 140 °C for $MA_2CuCl_2Br_2$ and 120 °C for $MA_2CuCl_{0.5}Br_{3.5}$, indicating a lower thermal stability for higher Br content and setting an upper limit to the annealing temperature (Figure S4, Supporting Information). The optimal annealing condition was found to be 70 °C for 1 h, since it resulted in highly crystalline perovskite without residual organic precursor. Higher temperatures (100 °C) caused decomposition of the perovskite structure, and lower annealing time (70 °C, 30 min) was not sufficient for complete reaction of methylammonium bromide MABr, as shown for $MA_2CuCl_{0.5}Br_{3.5}$ in Figure S5, Supporting Information.

The absorption spectra of the series $MA_2CuCl_xBr_{4-x}$ show typical features of copper complexes CuX_4^{2-} in square planar coordination[53−55] (Figure 2a), in agreement with the strong Jahn−Teller distortion observed in the XRD analysis. Strong bands for each material with absorption coefficients up to 35 000 cm^{-1} are found below 650 nm, and the corresponding band gaps determined from Tauc plots (Figure S6a, Supporting Information) are 2.48 eV (500 nm) for MA_2CuCl_4, 2.12 eV (584 nm) for $MA_2CuCl_2Br_2$, 1.90 eV (625 nm) for $MA_2CuClBr_3$, and 1.80 eV (689 nm) for $MA_2CuCl_{0.5}Br_{3.5}$.[56,57] The modulation of the band gap appears evident from the color of the powders, which changes from yellow to dark brown by increasing Br/Cl ratio (Figure 2c). Thermochromism was also observed for these bands, with a blue shift of the bandgap measured at low temperature (Figure S7, Supporting Information). Upon excitation at 310 nm, the perovskite films showed photoluminescence, which peaked around 515 nm with increasing intensity for higher Br/Cl ratio (Figure 2b). The observed green fluorescence can be assigned to the emission of Cu^+ ions[58] and suggests that Cu^{2+} is partially reduced during annealing creating emissive trap states in the material. The reduction process is strongly fostered by the presence of bromine, as suggested by the photoluminescence trend culminating in the stronger emission of $MA_2CuCl_{0.5}Br_{3.5}$, while chlorine helps to stabilize the Cu^{2+} oxidation state. This observation was confirmed by X-ray photoelectron spectroscopy (XPS) analysis, which also clearly revealed the presence of Cu^+ together with $CuCl_2$ in the perovskite films, with the Cu^+ content increasing with higher Br/Cl ratio (Figure S8, Supporting Information).

Table 1. Crystal Structure and Lattice Parameters[a] of Cu-Based Perovskites

formula	crystal system	space group	a [Å]	b [Å]	c [Å]	β [deg]	R_B
MA_2CuCl_4	monoclinic	(14) $P121/a1$	7.2574(8)	7.3504(1)	9.9688(5)	111.20	0.025
$MA_2CuCl_2Br_2$	orthorhombic	(64) *Acam*	7.3194(4)	7.3281(4)	19.1344(1)	90	0.021
$MA_2CuClBr_3$	orthorhombic	(64) *Acam*	7.3965(1)	7.3686(2)	19.3217(1)	90	0.013
$MA_2CuCl_{0.5}Br_{3.5}$	orthorhombic	(64) *Acam*	7.4276(2)	7.4686(8)	19.3075(9)	90	0.016

[a] $R_B = \sum_{hkl}|I_{hkl}(\text{obs}) - I_{hkl}(\text{calc})|/\sum_{hkl}|I_{hkl}(\text{obs})|$, where $I_{hkl} = mF_{hkl}^2$, (m = multiplicity).

DOI: 10.1021/acs.inorgchem.5b01896
Inorg. Chem. 2016, 55, 1044−1052

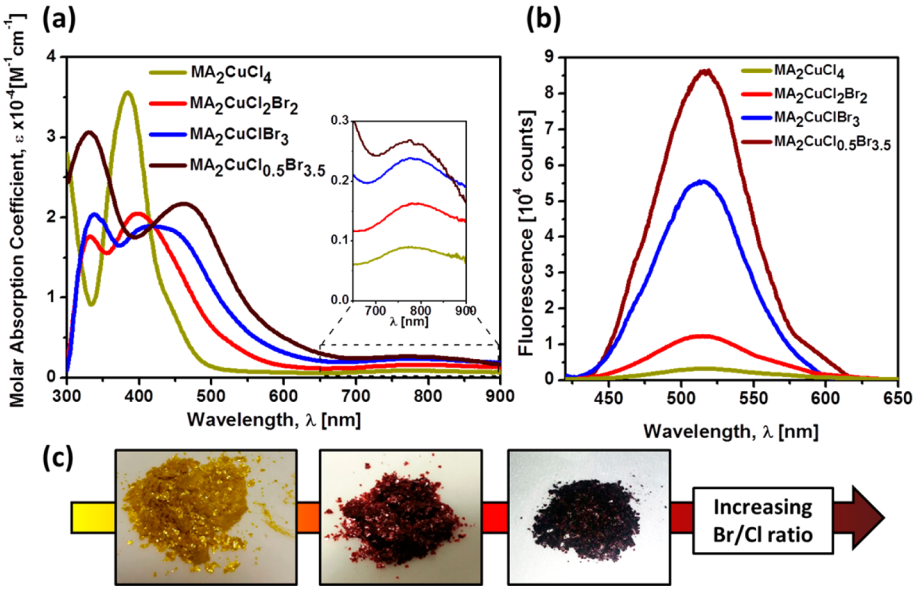

Figure 2. (a) Absorption coefficient for perovskites of the series $MA_2CuCl_xBr_{4-x}$ showing strong CT bands below 650 nm and broad d−d transitions between 700 and 900 nm (inset). (b) Photoluminescence of the perovskites $MA_2CuCl_xBr_{4-x}$ (λ exc =310 nm) with intensity increasing with higher Br contents; (c) color shift for powders with different Br/Cl ratio: MA_2CuCl_4 (yellow), $MA_2CuCl_2Br_2$ (red), $MA_2CuCl_{0.5}Br_{3.5}$ (dark brown).

The DFT method including on-site Coulomb interactions (DFT+U) was used to study the electronic structure of copper perovskite materials. These Cu^{2+}-ions containing compounds show the most stable ferromagnetic configuration within independent inorganic planes, while the interplanar coupling is anti-ferromagnetic (AFM_1), coinciding with previous electronic and magnetic studies of $(CH_3NH_3)_2CuCl_4$.[59] The trend of lower energies of the absorption peaks going from MA_2CuCl_4 to $MA_2CuClBr_{3.5}$ is in good agreement with our predicted band gap energies interpreted from band structures in Figure 3b,c and Figure S9, Supporting Information: MA_2CuCl_4 (3.09 eV), $MA_2CuCl_2Br_2$ (3.00 eV), $MA_2CuClBr_3$ (2.88 eV), and $MA_2CuCl_{0.5}Br_{3.5}$ (2.86 eV). Therefore, the position of these absorption bands is found to be highly dependent on the Br/Cl ratio, allowing the tuning of the band gap of these materials.

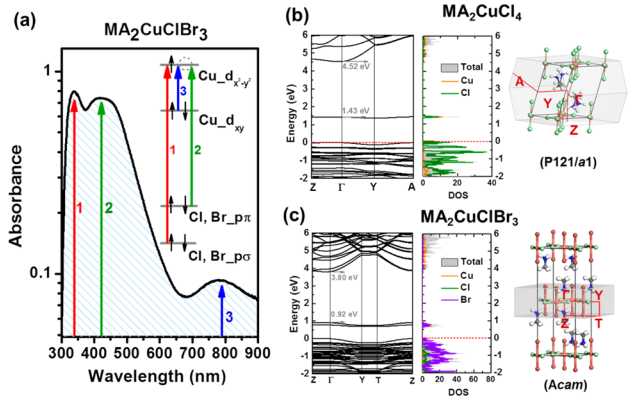

Figure 3. (a) Representation of the electronic transitions for $MA_2CuClBr_3$: charge-transfer transitions 1 and 2 (Cl, Br_pσ → Cu_$d_{x^2-y^2}$ and Cl, Br_pπ → Cu_$d_{x^2-y^2}$) and d−d transition 3 (Cu_d_{xy} → Cu_$d_{x^2-y^2}$; see Figure S11, Supporting Information for more details);electronic band structure, density of states, and unit cell structure of the perovskite compounds (b) MA_2CuCl_4 and (c) $MA_2CuClBr_3$ investigated by DFT simulation.

The strong bands (labeled as 1 and 2 in Figure 3a and S6b, exemplifying the electronic transitions for $MA_2CuClBr_3$ and $MA_2CuCl_2Br_2$, respectively) can be assigned to ligand-to-metal charge transfer (CT) transitions, as previously studied for $CuCl_4^{2-}$ complexes.[53] Specifically, from projected density of states (PDOS) of each atom (see Figure 3b,c), the bands 1 and 2 can be assigned to the transitions Cl, Br_pσ → Cu_$d_{x^2-y^2}$ and Cl, Br_pπ → Cu_$d_{x^2-y^2}$ and therefore are associated with CT states from ligand-related orbitals toward the highest antibonding of the d orbitals, namely, half-filled $d_{x^2-y^2}$. Interestingly, an additional contribution to the absorption is present below the band gap with weaker and broad bands between 700 and 900 nm (labeled as 3 in Figure 3a). This band can be assigned to d−d transitions within the d levels of Cu and does not shift for varying Br/Cl ratio across the series. The calculated PDOS of each orbital (Figure S10, Supporting Information) indicate transitions between the d orbitals of Cu, such as Cu_$d_{xz,\,yz}$ → Cu_$d_{x^2-y^2}$, Cu_d_{xy} → Cu_$d_{x^2-y^2}$, and Cu_d_{z^2} → Cu_$d_{x^2-y^2}$, in good agreement with previous reports on similar compounds based on square planar $CuCl_4^{2-}$ species.[60] A detailed analysis of the observed d−d transitions is given in Figure S11, Supporting Information. We note that all these materials have a very low density of states close to the band edge, which may reduce the probability of electronic transitions and be responsible for the lower absorption coefficient of these compounds compared to the standard lead-based perovskites.[61] Furthermore, the effective masses for holes and electrons were calculated, and the results are shown in Table 2. Strong anisotropy in the effective masses was found for all the material of this series, in agreement with their layered structure. The effective masses along the Γ-Z direction (inset in Figure 3b,c) are extremely high, especially in the case of the holes (indicated by ∞ in Table 2) as a consequence of the flat band structure. However, the effective masses in the Γ-Y direction (inset in Figure 3b,c) are much smaller, indicating that the charge transport is favored horizontally within the inorganic planes and hampered in the vertical direction. Moreover, while the electron effective mass in the Y-Z

DOI: 10.1021/acs.inorgchem.5b01896
Inorg. Chem. 2016, 55, 1044−1052

Table 2. Calculated Effective Mass for Hole and Electron of Copper Perovskite Compounds from Band Structure Using DFT+U Method

crystal structure	hole		electron	
	Γ-Z	Γ-Y	Γ-Z	Γ-Y
$(CH_3NH_3)_2CuCl_4$	∞	1.71	0.58	0.31
$(CH_3NH_3)_2CuCl_2Br_2$	∞	2.67	1.86	0.51
$(CH_3NH_3)_2CuClBr_3$	∞	1.51	2.39	0.57
$(CH_3NH_3)_2CuCl_{0.5}Br_{3.5}$	∞	1.55	4.04	0.52

direction is in the range of 0.31−0.57 and comparable to the case of $MAPbI_3$,[22] the hole effective mass is much higher (1.51−2.67) suggesting that the hole transport may be a main limitation to the charge transport in the material.

These 2D copper perovskites were integrated in a photovoltaic device architecture by infiltrating mesoporous titania (ms-TiO_2), as shown in the exploded view of the solar cell in Figure 4a. Here the perovskite is intended to act as a sensitizer, transferring an electron to the titania and a hole to the hole-transporting material (HTM) upon photoexcitation. Because of the low absorption coefficient found experimentally and in agreement with our DFT simulations, a thick screen-printed mesoporous layer was used to improve perovskite loading as well as the light harvesting. The perovskite was deposited by spin coating from DMSO solutions, with concentration optimized to obtain the best morphology. Good infiltration of the mesoporous layer was obtained with 1 and 2 M solutions, as shown in Figure S12, Supporting Information. In both of the cases, no capping layer was formed on top of the TiO_2. However, the faster crystallization achieved with the highest concentration produced less uniform films characterized by the prominent formation of isolated perovskite clusters discontinuously distributed across the film (Figure S12d, Supporting Information). In comparison, a much better infiltration was achieved with 1 M solutions that therefore were chosen for device fabrication. Figure 4b shows the cross section of a 5 μm mesoporous TiO_2 film infiltrated with $MA_2CuCl_2Br_2$ together with the energy dispersive X-ray (EDX) mapping of the Ti, Cu, Cl, and Br content. The perovskite appears to form huge crystalline regions interpenetrated with the mesoporous TiO_2 scaffold yielding a good filling of its porosity (Figure 4b,c). Moreover, the EDX mapping of Figure 4b,c additionally proves the homogeneous distribution and complete penetration of the perovskite across the whole depth of the mesoporous film.

Using spiro-MeOTAD as HTM and 5 μm mesoporous TiO_2, solar cell devices were fabricated with $MA_2CuCl_2Br_2$ and $MA_2CuCl_{0.5}Br_{3.5}$ and characterized (Figure 5a). $MA_2CuCl_2Br_2$ yielded a power conversion efficiency of 0.017%, with J_{sc} = 216 $\mu A/cm^2$, V_{oc} = 256 mV, and FF = 0.32. Despite the optimized band gap, $MA_2CuCl_{0.5}Br_{3.5}$ gave a much lower power conversion efficiency of 0.0017%, J_{sc} = 21 $\mu A/cm^2$, V_{oc} = 290 mV, and FF = 0.28. The lower performance of $MA_2CuCl_{0.5}Br_{3.5}$ can be explained with the higher trap density introduced by Cu^{2+} reduction (as confirmed by XPS and photoluminescence measurements), which introduce an additional pathway for charge recombination. The dark current for the two devices was probed in a wider range from −4 to +4 V to confirm the rectifying behavior of the cell operating under dark condition (Figure S13, Supporting Information). The high dark currents observed (Figure 5a and Figure S13, Supporting Information) suggest the presence of high leakage current possibly due to the direct contact between the TiO_2 and HTM, facilitated by the absence of perovskite capping layer over the mesoporous TiO_2. As additional limitation factor, ultraviolet photoelectron spectroscopy (UPS) measurements (Figure S14, Supporting Information) revealed a mismatch between the valence band maximum (VBM) of $MA_2CuCl_2Br_2$ (−4.98 eV) and highest occupied molecular orbital level of spiro-MeOTAD (−5.2 eV),[62] suggesting poor hole transfer in the device. Photocurrent measurements were performed on the device based on $MA_2CuCl_2Br_2$ and proved the sensitization action of the perovskite (Figure 5b). The measurement was performed using a conventional amplitude modulation technique, a Xe lamp as

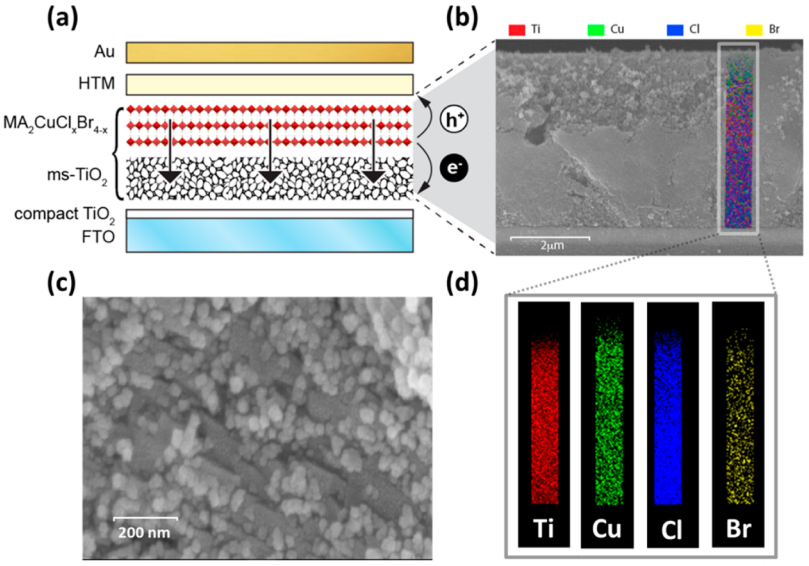

Figure 4. (a) Exploded view of solar cell devices based on mesoporous TiO_2 sensitized with the perovskite $MA_2CuCl_xBr_{4-x}$; (b) cross section of a mesoporous TiO_2 layer (5 μm) with EDX mapping showing the homogeneous infiltration with 2D copper perovskite $MA_2CuCl_2Br_2$ along all the film depth; (c) higher magnification of perovskite effectively filling the pores of the TiO_2 scaffold; (d) EDX mapping of the distribution of the individual elements Ti, Cu, Cl, Br along the cross section of the film.

DOI: 10.1021/acs.inorgchem.5b01896
Inorg. Chem. 2016, 55, 1044−1052

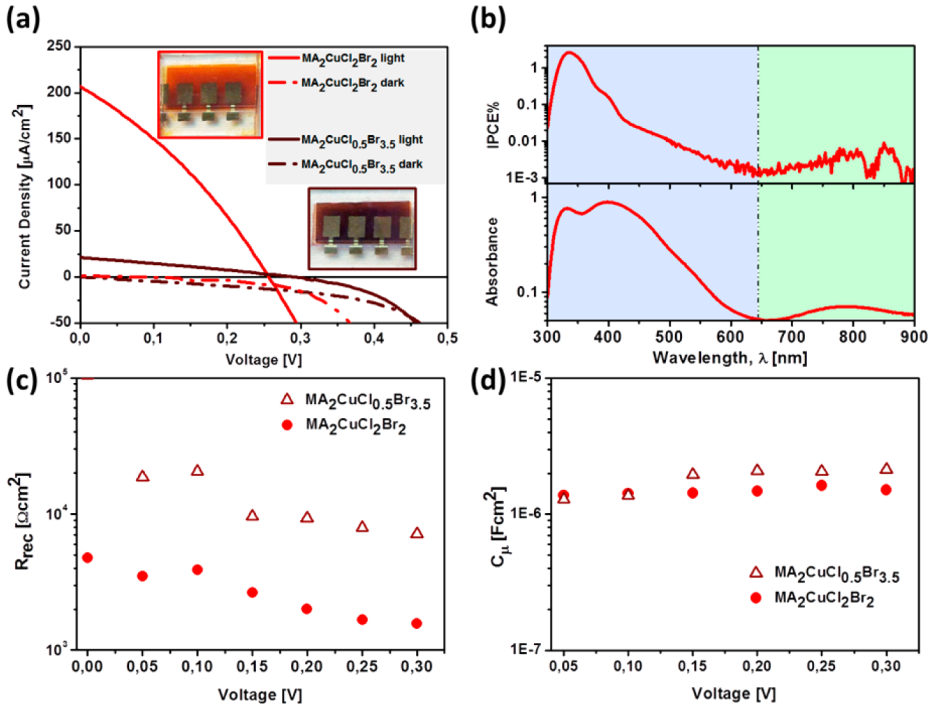

Figure 5. (a) $I-V$ curve of solar cells sensitized with $MA_2CuCl_2Br_2$ (red) and $MA_2CuCl_{0.5}Br_{3.5}$ (brown) under 1 sun of light illumination. The dashed red and brown lines represent the dark current; (b) photocurrent measurement performed on a device sensitized with $MA_2CuCl_2Br_2$ (upper) compared to the perovskite absorption spectrum. (c) Recombination resistance and (d) chemical capacitance extracted from the fitting of the IS spectra measured under 1 sun of illumination.

white light source, and a monochromator to disperse the light in the 300−900 nm spectral region. Both CT and d−d transitions contribute to the photoresponsivity: while the major photoresponse is due to CT transitions of the perovskite below 650 nm, a weak photocurrent signal between 700 and 900 nm is also detected, indicating that d−d transitions may be effectively exploited for photocurrent generation.

To elucidate the differences between these two samples, impedance spectroscopy (IS) was measured under illumination in the working voltage range of the devices. The IS spectrum (Figure S15a, Supporting Information) features one single arc with high resistivity, suggesting a response dominated by a CT process rather than a charge transport one. From the fittings (following the equivalent circuit shown in the inset of Figure S15a, Supporting Information) it is possible to estimate the series (R_s, Figure S15b, Supporting Information) and parallel resistances as well as the capacitance. The parallel resistance, attributed to the recombination process (R_{rec}), shows a lower value (indicative of higher recombination) for the $MA_2CuCl_2Br_2$ sample (Figure 5c). The higher recombination resistance can explain the slightly higher V_{oc} achieved by the $MA_2CuCl_{0.5}Br_{3.5}$ sample, despite its much lower current. It is worth to remark that the large values of the recombination resistance indicate that the CT process is hampered as well, hindering the photogenerated charge injection and contributing to the low currents achieved. The values obtained for the capacitance stand in the range of a classical chemical capacitance (C_μ) of TiO_2[63] (Figure 5d). This, along with the similar C_μ obtained for both analyzed devices, confirms charge injection from the absorber to the mesoporous semiconductor, unlike other perovskite solar cells.[64]

According to our analysis, the solar cells are limited by the combination of low absorption coefficient (as compared to the standard $MAPbI_3$), strong anisotropy in the charge-transport properties, and heavy mass for the holes. The poor photovoltaic efficiency results from the tradeoff between the thickness of the films required to achieve reasonable light harvesting in the cell and the limited charge diffusion (due to the large confinement in the 2D structure and the unfavorable orientation toward the 00l direction). This is especially evident in solar cells with planar structure, where the vertical charge transport is strongly hampered due to the preferential orientation of the perovskite toward the 00l direction and the heavy hole and electron effective masses for transport in the Γ-Z direction of reciprocal space. This was confirmed by the extremely low current density (J_{sc} = 342 nA/cm^2) achieved with a planar device having structure ITO/PEDOT:PSS/$MA_2CuCl_2Br_2$/PCBM/Al (Figure S16, Supporting Information). Therefore, the use of mesoporous TiO_2 layer allows the disruption of the continuous 2D perovskite structure, helping the charge extraction from the material as well as the vertical charge transport in the device. Formation of Cu^+ trap states during the film processing further creates obstacles for the achievement of higher efficiency, but the efficient luminescence coming from in situ formed Cu^+ ions may be exploited for lead-free perovskite-based light-emitting devices.

This work is the first example of application of 2D "green" perovskites based on a transition metal as light harvester in solar cells and represents a proof of concept for their application as photovoltaic materials. The area of 2D perovskites remains critically important especially for the pursuit of Pb-free perovskites for light-emitting and photovoltaic applications. 2D perovskites allow for a wider tuning of the composition,[37] due to the relaxed geometrical constraints. Such structures allow the incorporation of a wider variety of metal atoms and long-chain organic cations to form tunable

DOI: 10.1021/acs.inorgchem.5b01896
Inorg. Chem. 2016, 55, 1044−1052

multiquantum well structures. To overcome the aforementioned limitations, our study highlights the importance to include optoelectronically active organic cations to overcome the issues due to the intrinsic layered structure of these materials, especially to increase optical absorption cross section and improve mobility and vertical charge transport. The use of active aromatic cations such as tropylium[65] $[C_7H_7]^+$ and oligothiophene chromophores[66] for formation of hybrid perovskites have already been shown, and their combination with transition metals will certainly improve the optoelectronic properties of these hybrid materials. Controlled crystal growth to achieve an orthogonal alignment of the perovskite layers on the substrate is also desirable to facilitate charge drain and collection at the counter electrodes. Moreover, p-type DSSC architectures based on mesoporous p-type oxides (e.g., NiO) sensitized with copper perovskites may be a viable route to overcome the hole transport issues related to the high hole effective masses.[67,68] Thanks to the ease of formation, stability in aerobic environment and absorption up to the NIR region, hybrid copper perovskites are an optimal platform to investigate these further developments.

CONCLUSIONS

The 2D perovskite series $MA_2CuCl_xBr_{4-x}$ was studied in detail, and material stability and optical properties were shown to be strongly dependent on the Br/Cl ratio. The absorption is dominated by ligand-to-metal CT transitions (Cl, Br_pσ → Cu_$d_{x^2-y^2}$ and Cl, Br_pπ → Cu_$d_{x^2-y^2}$), and their associated band gap can be tuned increasing the Br content from 2.48 eV (500 nm) for MA_2CuCl_4 to 1.80 eV (689 nm) for $MA_2CuCl_{0.5}Br_{3.5}$. An additional contribution to the absorption in the region between 700 and 900 nm comes from Cu_d_{xy} → Cu_$d_{x^2-y^2}$ transitions within the d Cu levels. These perovskites can be easily deposited in thin films by spin coating, forming highly oriented films toward the 00l direction. Cu^{2+} reduction during annealing is favored by the presence of Br^-, and the in situ formed Cu^+ ions were found to be responsible for the significantly increased green photoluminescence intensity at 515 nm with higher Br/Cl ratio. These emission properties are also promising for possible applications of these materials in light-emitting devices. Solar cell devices based on copper perovskite were realized: the uniform infiltration of mesoporous titania with 2D copper perovskites was achieved, and power conversion efficiency of 0.017% was obtained using $MA_2CuCl_2Br_2$ as sensitizer. Moreover, both the CT and d−d transitions were shown to actively contribute to the photocurrent generation, demonstrating for the first time the potential photovoltaic properties of this class of Cu-based 2D perovskites. Although the TiO_2 mesoporous scaffold has been shown to help the electron extraction from the 2D perovskite, we found that the combination of low absorption coefficient and heavy mass for the holes compromise the solar cell efficiency. The introduction of optoelectronically active cations is expected to overcome these issues stressing the importance of investigation of novel hybrid materials and making 2D copper-based hybrid perovskites an ideal platform to study these further developments.

EXPERIMENTAL SECTION

Synthesis of $MA_2CuCl_xBr_{4-x}$ Perovskite Powders. Methylammonium chloride MACl and methylammonium bromide MABr were synthesized by mixing 16.7 and 18.0 mL of methylamine solution (CH_3NH_2, 40% in methanol) with 11.3 mL of hydrochloric acid HCl (37 wt % in water) and 8.0 mL of hydrobromic acid HBr (48% in water, Sigma-Aldrich), respectively. The white powders obtained were purified by crystallization from EtOH with diethyleter and dried in vacuum oven (12 h, 60 °C).

Perovskite powders MA_2CuCl_4, $MA_2CuCl_2Br_2$, $MA_2CuClBr_3$, $MA_2CuCl_{0.5}Br_{3.5}$, and MA_2CuBr_4 were synthesized from ethanol solutions. The precursors MACl, MABr, $CuCl_2$ (copper chloride, 99% Sigma-Aldrich), and $CuBr_2$ (copper bromide, 99% Sigma-Aldrich) were mixed in the desired stoichiometry (1.2 equiv of organic precursors were used to ensure the complete reaction of the inorganic salts). For example, to obtain $MA_2CuCl_{0.5}Br_{3.5}$, 2.68 g of $CuBr_2$, 2.42 g of MABr, and 0.48 g of MACl were mixed in 100 mL of EtOH, stirred for 2 h at 60 °C, and left to crystallize overnight in an ice bath. The product was recovered by filtration, dried at 60 °C for 12 h in vacuum oven, and stored in glovebox. Spontaneous crystallization from solution did not occur for MA_2CuBr_4, which was only obtained after complete evaporation of the solvent.

Material Characterization. BRUKER D8 ADVANCE with Bragg−Brentano geometry was used for X-ray analysis, with Cu Kα radiation (λ = 1.540 56 Å), step increment of 0.02°, and 1 s of acquisition time. An air-sensitive sample holder was used for thin-film characterization. The software TOPAS 3.0 was used for XRD data analysis.[69] The Pawley fitting for $(CH_3NH_3)_2CuCl_4$ and $(CH_3N_3)_2$-$CuCl_xBr_{4-x}$ was done starting from the structural data reported in ICSD No. 110687 and ICSD No. 110677, while the parameters reported by Y. Kimishima were used for MA_2CuBr_4.[46] The data fitting was done using the fundamental parameters approach.[70] Peak profile and background were fit, respectively, with a TCHZ Pseudo-Voigt function and a Chebichev polynomial of fifth order with $1/x$ function. The refined parameters were the zero error, scale factor, linear absorption coefficient, and lattice parameters. Diamond 3.2 software was used to draw the crystal structure.

X-ray photoelectron spectroscopy measurements were done using monochromatic X-ray source from Al Kα ($h\nu$ = 1486.7 eV) and a hemispherical analyzer (EA125, Omicron). To eliminate air-induced change to Cu perovskite samples, a direct transfer method (direct transfer from glovebox to vacuum condition) is used to avoid air contact during sample transfer.

Morphological and compositional characterization was done with a field emission scanning electron microscope (FE-SEM) coupled with an energy dispersive X-ray analysis (EDX) Jeol JSM-6700F.

The instrument 2950 TGA HR V5.4 (TA Instruments) was used for the TGA. The analysis was performed under nitrogen (flow rate 40 mL/min), and an interval from 30 to 900 °C (ramp rate 5 °C/min) was studied.

A UV−vis−NIR spectrophotometer (UV3600, Shimadzu) was used for optical characterization. Absorption spectra were measured on perovskite thin films deposited by spin coating on glass slides from DMSO solutions of the perovskite powders and protected against moisture with poly(methyl methacrylate) layers. To calculate the molar absorption coefficients, the thickness of the film was measured with the surface profiler Alpha-Step IQ. Photoluminescence was measured using the spectrofluorometer Fluorolog-3 (Horiba, Jobin Yvon) on films deposited on silicon substrates.

Computational Methods. All the structural optimization and electronic structure calculations were performed by the QUANTUM ESPRESSO code[71] in the framework of DFT. The general gradient approximation functional of Perdew−Burke−Ernzerhof[72] was employed. Electron−ion interactions were described by ultrasoft pseudopotentials with electrons from H (1s); O, N, and C (2s, 2p); Cl (3s, 3p); Br (4s, 4p); Cu (3s, 3p, 3d, 4s, 4p), shells explicitly included in the calculations.[73] Single-particle wave functions (charges) were expanded on a plane-wave basis set up to a kinetic energy cutoff of 50 Ry (300 Ry) and k-point mesh of 4 × 4 × 4 for MA_2CuCl_4 and 4 × 4 × 2 for $MA_2CuCl_2Br_2$, $MA_2CuClBr_3$, $MA_2CuCl_{0.5}Br_{3.5}$ were chosen here considering accurate and computational point. The experimental crystal structures of monoclinic or orthorhombic coordinates at room temperature were used as an initial guess. The atomic relaxation calculations were performed by fixing the Cu atoms and allowing other atoms to relax until the residual atomic forces are

DOI: 10.1021/acs.inorgchem.5b01896
Inorg. Chem. 2016, 55, 1044−1052

less than 0.002 eV/Å. The approach to the DFT+U method introduced by Dudarev et al.[74] was used in all calculations to include the strongly correlated effects on the d states of Cu, and the on-site Coulomb interaction parameter (U = 7.5 eV) was adopted in our calculations. The effective masses for hole and electron were calculated by fitting of the dispersion relation of $m^* = \frac{\hbar^2}{\partial^2 E(k) / \partial^2 k}$ from the band structures in Figure 3 along the Γ-Z and Γ-Y directions.

Solar Cell Fabrication. *Mesoporous Structure.* Fluorine-doped tin oxide (FTO) glass substrates were cleaned with sonication in decon soap, deionized H_2O, and ethanol each for 30 min. Spray pyrolysis was used to deposit the compact TiO_2 blocking layer using a precursor solution of titanium diisopropoxide bis(acetylacetonate); then the substrates were treated with 0.1 M $TiCl_4$ solution at 70 °C for 1 h. Mesoporous TiO_2 layers (5 μm) were screen printed using the paste DSL30NRD (Dyesol) and sintered at 500 °C. DMSO solutions (1 M) were prepared dissolving the preformed perovskite powders and spin-coated with the following parameters: 500 rpm, 30 s−1000 rpm, 30 s−4000 rpm, 180 s. The annealing was done on a hot plate at 70 °C for 1 h. Spiro-MeOTAD was spin-coated from chlorobenzene solution (180 mg/mL) at 4000 rpm for 30 s. No additives to the hole transporter layer were employed during this study. Gold electrodes were deposited by thermal evaporation, defining an active area of the solar cell of 0.2 cm^2. Perovskite, spiro-MeOTAD and gold deposition were performed in glovebox.

Planar Structure. Indium tin oxide (ITO) glass substrates were etched using zinc powder and diluted HCl, cleaned and exposed to oxygen plasma for 2 min. Poly(3,4-ethylenedioxythiophene) polystyrenesulfonate (PEDOT:PSS) was deposited from water solution at 3000 rpm, 60 s and annealed on hot plate (125 °C, 20 min). Under N_2 atmosphere, 1 M DMSO solution of $(CH_3NH_3)_2CuCl_2Br_2$ was then spin coated with steps 500 rpm, 30 s−1000 rpm, 30 s−4000, and the film was annealed at 70 °C for 1 h. PCBM was spin coated from 20 mg/mL chloroform/chlorobenzene 1:1 solutions at 1000 rpm for 50 s, and aluminum electrodes were finally deposited defining an active area of 0.07 cm^2.

Solar Cell Characterization. The current−voltage characteristics were measured using an Agilent 4155C analyzer and under AM 1.5G simulated illumination from a solar simulator (San-EI Electric, XEC-301S). Masks with the same area of the metal electrodes were applied on the front face of the cells during the measurement.

Photocurrent Measurements. The responsivity was calculated according to the equation $R_i = \frac{i_{ph}}{P_{in}}$, where P_{in} is the light power incident onto the surface of the sample, and i_{ph} is the measured photocurrent. The responsivity was measured with conventional amplitude modulation technique using a Xe lamp as white light source and a monochromator to disperse the light within the range from 300 to 900 nm. The modulation was done using a mechanical chopper at frequency of 138 Hz, and the monochromatic light intensity was determined by a calibrated reference photodiode. Time constant of the lock-in amplifier was set to 300 ms, which corresponds to 0.42 Hz equivalent noise bandwidth.

IMPEDANCE SPECTROSCOPY

The measurements were performed inside a N_2-filled glovebox with an Autolab PGSTAT128N. Under 1 sun of illumination, a 20 mV perturbation was applied with frequencies varying from 200 kHz to 1 Hz and direct current voltages varying from 0 to 300 mV.

ASSOCIATED CONTENT

Supporting Information

The Supporting Information is available free of charge on the ACS Publications website at DOI: 10.1021/acs.inorgchem.5b01896.

XRD, TGA, XPS, and UPS data, $I-V$ curve of inverted structure cell, density of states based on DFT simulation, SEM images, work function determination, impedance analysis, as well as morphological and optical characterization details (d−d transitions and temperature dependent absorption). (PDF)

AUTHOR INFORMATION

Corresponding Author

*E-mail: Nripan@ntu.edu.sg.

Notes

The authors declare no competing financial interest.

ACKNOWLEDGMENTS

We acknowledge S. Shukla and N. Yantara for the assistance in the fabrication and characterization and T. Krishnamoorthy for TGA measurements. The Singapore-Berkeley Research Initiative for Sustainable Energy Create Programme is gratefully acknowledged for financial support. We also acknowledge funding from National Research Foundation (NRF) Singapore (Program #: NRF-CRP14-2014-03).

REFERENCES

(1) Kamat, P. V. *J. Am. Chem. Soc.* **2014**, *136*, 3713−3714.
(2) Kim, H.-S.; Im, S. H.; Park, N.-G. *J. Phys. Chem. C* **2014**, *118*, 5615−5625.
(3) Kojima, A.; Teshima, K.; Shirai, Y.; Miyasaka, T. *J. Am. Chem. Soc.* **2009**, *131*, 6050−6051.
(4) Im, J.-H.; Lee, C.-R.; Lee, J.-W.; Park, S.-W.; Park, N.-G. *Nanoscale* **2011**, *3*, 4088−4093.
(5) Kim, H.-S.; Lee, C.-R.; Im, J.-H.; Lee, K.-B.; Moehl, T.; Marchioro, A.; Moon, S.-J.; Humphry-Baker, R.; Yum, J.-H.; Moser, J. E.; Grätzel, M.; Park, N.-G. *Sci. Rep.* **2012**, *2*, 591.
(6) Liu, M.; Johnston, M. B.; Snaith, H. J. *Nature* **2013**, *501*, 395−398.
(7) Hu, Q.; Wu, J.; Jiang, C.; Liu, T.; Que, X.; Zhu, R.; Gong, Q. *ACS Nano* **2014**, *8*, 10161−10167.
(8) Nie, W.; Tsai, H.; Asadpour, R.; Blancon, J.-C.; Neukirch, A. J.; Gupta, G.; Crochet, J. J.; Chhowalla, M.; Tretiak, S.; Alam, M. A.; Wang, H.-L.; Mohite, A. D. *Science* **2015**, *347*, 522−525.
(9) Liu, D.; Kelly, T. L. *Nat. Photonics* **2014**, *8*, 133−138.
(10) Burschka, J.; Pellet, N.; Moon, S.-J.; Humphry Baker, R.; Gao, P.; Nazeeruddin, M.; Graetzel, M. *Nature* **2013**, *499*, 316−319.
(11) Green, M. A.; Emery, K.; Hishikawa, Y.; Warta, W.; Dunlop, E. D. *Prog. Photovoltaics* **2014**, *22*, 701−710.
(12) Zhang, W.; Saliba, M.; Moore, D. T.; Pathak, S. K.; Hörantner, M. T.; Stergiopoulos, T.; Stranks, S. D.; Eperon, G. E.; Alexander-Webber, J. A.; Abate, A.; Sadhanala, A.; Yao, S.; Chen, Y.; Friend, R. H.; Estroff, L. A.; Wiesner, U.; Snaith, H. J. *Nat. Commun.* **2015**, *6*, 614210.1038/ncomms7142
(13) Boix, P. P.; Nonomura, K.; Mathews, N.; Mhaisalkar, S. G. *Mater. Today* **2014**, *17*, 16−23.
(14) Xing, G.; Mathews, N.; Lim, S.; Yantara, N.; Liu, X.; Sabba, D.; Graetzel, M.; Mhaisalkar, S.; Sum, T. *Nat. Mater.* **2014**, *13*, 476−480.
(15) Xing, G.; Mathews, N.; Sun, S.; Lim, S.; Lam, Y.; Graetzel, M.; Mhaisalkar, S.; Sum, T. *Science* **2013**, *342*, 344−347.
(16) Zhou, H.; Chen, Q.; Li, G.; Luo, S.; Song, T.-b.; Duan, H.-S.; Hong, Z.; You, J.; Liu, Y.; Yang, Y. *Science* **2014**, *345*, 542−546.
(17) Gao, P.; Gratzel, M.; Nazeeruddin, M. K. *Energy Environ. Sci.* **2014**, *7*, 2448−2463.
(18) Snaith, H. *J. Phys. Chem. Lett.* **2013**, *4*, 3623−3630.
(19) Green, M. A.; Ho-Baillie, A.; Snaith, H. J. *Nat. Photonics* **2014**, *8*, 506−514.
(20) Stranks, S. D.; Snaith, H. J. *Nat. Nanotechnol.* **2015**, *10*, 391−402.
(21) Tan, Z.-K.; Moghaddam, R. S.; Lai, M. L.; Docampo, P.; Higler, R.; Deschler, F.; Price, M.; Sadhanala, A.; Pazos, L. M.; Credgington,

DOI: 10.1021/acs.inorgchem.5b01896
Inorg. Chem. 2016, 55, 1044−1052

D.; Hanusch, F.; Bein, T.; Snaith, H. J.; Friend, R. H. *Nat. Nanotechnol.* **2014**, *9*, 687−692.
(22) Chin, X. Y.; Cortecchia, D.; Yin, J.; Bruno, A.; Soci, C. *Nat. Commun.* **2015**, *6*, 7383.
(23) You, J.; Hong, Z.; Yang, Y.; Chen, Q.; Cai, M.; Song, T.-B.; Chen, C.-C.; Lu, S.; Liu, Y.; Zhou, H.; Yang, Y. *ACS Nano* **2014**, *8*, 1674−1680.
(24) Eperon, G. E.; Burlakov, V. M.; Goriely, A.; Snaith, H. J. *ACS Nano* **2013**, *8*, 591−598.
(25) Li, Y.; Moon, K.-s.; Wong, C. P. *Science* **2005**, *308*, 1419−1420.
(26) Panda, P. K. *J. Mater. Sci.* **2009**, *44*, 5049−5062.
(27) Goyer, R. A. *Environ. Health Perspect* **1993**, *100*, 177−187.
(28) Slaveykova, V. I.; Wilkinson, K. J. *Environ. Sci. Technol.* **2002**, *36*, 969−975.
(29) Kumar, M. H.; Dharani, S.; Leong, W. L.; Boix, P. P.; Prabhakar, R. R.; Baikie, T.; Shi, C.; Ding, H.; Ramesh, R.; Asta, M.; Graetzel, M.; Mhaisalkar, S. G.; Mathews, N. *Adv. Mater.* **2014**, *26*, 1−6.
(30) Hao, F.; Stoumpos, C. C.; Cao, D. H.; Chang, R. P. H.; Kanatzidis, M. G. *Nat. Photonics* **2014**, *8*, 489−494.
(31) Chung, I.; Lee, B.; He, J.; Chang, R. P. H.; Kanatzidis, M. G. *Nature* **2012**, *485*, 486−489.
(32) Noel, N. K.; Stranks, S. D.; Abate, A.; Wehrenfennig, C.; Guarnera, S.; Haghighirad, A.-A.; Sadhanala, A.; Eperon, G. E.; Pathak, S. K.; Johnston, M. B.; Petrozza, A.; Herz, L. M.; Snaith, H. J. *Energy Environ. Sci.* **2014**, *7*, 3061−3068.
(33) Cheng, Z.; Lin, J. *CrystEngComm* **2010**, *12*, 2646−2662.
(34) Moodenbaugh, A. R.; Suenaga, M.; Folkerts, T. J.; Shelton, R. N.; Xu, Y. *Phys. Rev. B: Condens. Matter Mater. Phys.* **1988**, *38*, 4596−4600.
(35) Mitzi, D. B. Hybrid Organic-Inorganic Electronics. In *Functional Hybrid Materials;* Wiley-VCH Verlag GmbH & Co. KGaA: 2005; pp 347−386.
(36) Mitzi, D. B. *J. Chem. Soc., Dalton Trans.* **2001**, 1−12.
(37) Mitzi, D. B., Synthesis, Structure, and Properties of Organic-Inorganic Perovskites and Related Materials. In *Progress in Inorganic Chemistry;* John Wiley & Sons, Inc: 2007; pp 1−121.
(38) Greenwood, N. N.; Earnshaw, A. *Chemistry of the elements;* Pergamon Press: 1984.
(39) Willett, R.; Place, H.; Middleton, M. *J. Am. Chem. Soc.* **1988**, *110*, 8639−8650.
(40) Snively, L. O.; Drumheller, J. E.; Emerson, K. *Phys. Rev. B: Condens. Matter Mater. Phys.* **1981**, *23*, 6013−6017.
(41) de Jongh, L. J. *J. Appl. Phys.* **1978**, *49*, 1305−1310.
(42) Estes, W. E.; Losee, D. B.; Hatfield, W. E. *J. Chem. Phys.* **1980**, *72*, 630−638.
(43) Jaffe, A.; Karunadasa, H. I. *Inorg. Chem.* **2014**, *53*, 6494−6496.
(44) Smith, I. C.; Hoke, E. T.; Solis-Ibarra, D.; McGehee, M. D.; Karunadasa, H. I. *Angew. Chem.* **2014**, *126*, 11414−11417.
(45) Im, J. H.; Chung, J.; Kim, S. J.; Park, N. G. *Nanoscale Res. Lett.* **2012**, *7*, 353.
(46) Kimishima, Y. *J. Phys. Soc. Jpn.* **1980**, *49*, 62−66.
(47) Pabst, I.; Fuess, H.; Bats, J. W. *Acta Crystallogr., Sect. C: Cryst. Struct. Commun.* **1987**, *43*, 413−416.
(48) Willett, R. *Acta Crystallogr., Sect. C: Cryst. Struct. Commun.* **1991**, *47*, 1081−1082.
(49) Suzuki, Y.; Kubo, H. *J. Phys. Soc. Jpn.* **1983**, *52*, 1420−1426.
(50) Li, C.; Lu, X.; Ding, W.; Feng, L.; Gao, Y.; Guo, Z. *Acta Crystallogr., Sect. B: Struct. Sci.* **2008**, *64*, 702−707.
(51) Li, C.; Soh, K. C. K.; Wu, P. *J. Alloys Compd.* **2004**, *372*, 40−48.
(52) Cohen, B. N.; Labarca, C.; Davidson, N.; Lester, H. A. *J. Gen. Physiol.* **1992**, *100*, 373−400.
(53) Desjardins, S. R.; Penfield, K. W.; Cohen, S. L.; Musselman, R. L.; Solomon, E. I. *J. Am. Chem. Soc.* **1983**, *105*, 4590−4603.
(54) Valiente, R.; Rodríguez, F. *Phys. Rev. B: Condens. Matter Mater. Phys.* **1999**, *60*, 9423−9429.
(55) Jaffe, A.; Lin, Y.; Mao, W. L.; Karunadasa, H. I. *J. Am. Chem. Soc.* **2015**, *137*, 1673−1678.
(56) Boix, P. P.; Agarwala, S.; Koh, T. M.; Mathews, N.; Mhaisalkar, S. G. *J. Phys. Chem. Lett.* **2015**, *6*, 898−907.
(57) Cortecchia, D.; Dewi, H. A.; Dharani, S.; Baikie, T.; Soci, C.; Mathews, N. Green 2D Hybrid Perovskites for Perovskite-Based Solar Cells. In *EOSAM 2014;* European Optical Society: Berlin, Germany, 2014.
(58) Gomez, S.; Urra, I.; Valiente, R.; Rodriguez, F. *J. Phys.: Condens. Matter* **2010**, *22*, 295505.
(59) Zolfaghari, P.; de Wijs, G. A.; de Groot, R. A. *J. Phys.: Condens. Matter* **2013**, *25*, 295502.
(60) Willett, R. D.; Liles, O. L.; Michelson, C. *Inorg. Chem.* **1967**, *6*, 1885−1889.
(61) Yin, W.-J.; Shi, T.; Yan, Y. *Adv. Mater.* **2014**, *26*, 4653−4658.
(62) Schulz, P.; Edri, E.; Kirmayer, S.; Hodes, G.; Cahen, D.; Kahn, A. *Energy Environ. Sci.* **2014**, *7*, 1377−1381.
(63) Fabregat-Santiago, F.; Garcia-Belmonte, G.; Mora-Sero, I.; Bisquert, J. *Phys. Chem. Chem. Phys.* **2011**, *13*, 9083−9118.
(64) Dharani, S.; Dewi, H. A.; Prabhakar, R. R.; Baikie, T.; Shi, C.; Yonghua, D.; Mathews, N.; Boix, P. P.; Mhaisalkar, S. G. *Nanoscale* **2014**, *6*, 13854−13860.
(65) Maughan, A. E.; Kurzman, J. A.; Neilson, J. R. *Inorg. Chem.* **2015**, *54*, 370−378.
(66) Mitzi, D. B.; Chondroudis, K.; Kagan, C. R. *Inorg. Chem.* **1999**, *38*, 6246−6256.
(67) Zhu, H.; Hagfeldt, A.; Boschloo, G. *J. Phys. Chem. C* **2007**, *111*, 17455−17458.
(68) Borgström, M.; Blart, E.; Boschloo, G.; Mukhtar, E.; Hagfeldt, A.; Hammarström, L.; Odobel, F. *J. Phys. Chem. B* **2005**, *109*, 22928−22934.
(69) Bruker. *Topas,* Version 4.1; Bruker AXS Inc: Madison, WI, 2008.
(70) Cheary, R. W.; Coelho, A. *J. Appl. Crystallogr.* **1992**, *25*, 109−121.
(71) Giannozzi, P.; Baroni, S.; Bonini, N.; Calandra, M.; Car, R.; Cavazzoni, C.; Ceresoli, D.; Chiarotti, G. L.; Cococcioni, M.; Dabo, I.; Dal Corso, A.; de Gironcoli, S.; Fabris, S.; Fratesi, G.; Gebauer, R.; Gerstmann, U.; Gougoussis, C.; Kokalj, A.; Lazzeri, M.; Martin-Samos, L.; Marzari, N.; Mauri, F.; Mazzarello, R.; Paolini, S.; Pasquarello, A.; Paulatto, L.; Sbraccia, C.; Scandolo, S.; Sclauzero, G.; Seitsonen, A. P.; Smogunov, A.; Umari, P.; Wentzcovitch, R. M. *J. Phys.: Condens. Matter* **2009**, *21*, 395502. DOI: 10.1088/0953-8984/21/39/395502
(72) Perdew, J. P.; Burke, K.; Ernzerhof, M. *Phys. Rev. Lett.* **1996**, *77*, 3865−3868.
(73) Garrity, K. F.; Bennett, J. W.; Rabe, K. M.; Vanderbilt, D. *Comput. Mater. Sci.* **2014**, *81*, 446−452.
(74) Dudarev, S. L.; Botton, G. A.; Sutton, A. P. *14th International Congress on Electron Microscopy* **1998**, *3*, 613−614.

DOI: 10.1021/acs.inorgchem.5b01896
Inorg. Chem. 2016, 55, 1044−1052